Article

Comparison of *Ratioing* and *RCNA* Methods in the Detection of Flooded Areas Using Sentinel 2 Imagery (Case Study: Tulun, Russia)

Helena Maria Fernandez [1,2], Fernando Granja-Martins [1,2], Olga Dziuba [3], David A. B. Pereira [1] and Jorge M. G. P. Isidoro [1,4,*]

[1] Department of Civil Engineering, Institute of Engineering, University of Algarve, Campus da Penha, 8005-139 Faro, Portugal; hfernand@ualg.pt (H.M.F.); fmmartin@ualg.pt (F.G.-M.); dpereira@ualg.pt (D.A.B.P.)

[2] Centre for Research in Tourism, Sustainability and Well-Being (CinTurs), Universidade do Algarve, 8005-139 Faro, Portugal

[3] Faculty of Sciences and Technology, University of Algarve, Campus de Gambelas, 8005-139 Faro, Portugal; olgadziuba86@gmail.com

[4] MARE—Marine and Environmental Sciences Centre/ARNET—Aquatic Research NETwork, Rua da Matemática, 49, 3004-517 Coimbra, Portugal

[*] Correspondence: jisidoro@ualg.pt

Abstract: Climate change and natural disasters caused by hydrological, meteorological, and climatic phenomena have a significant impact on cities. Russia, a continental country with a vast territory of complex geographic–ecological environments and highly variable climatic conditions, is subject to substantial and frequent natural disasters. On 29 June 2019, an extreme precipitation event occurred in the city of Tulun in the Irkutsk oblast, Russian Federation, which caused flooding due to the increase in the water level of the Iya River that passes through the city, leaving many infrastructures destroyed and thousands of people affected. This study aims to determine the flooded areas in the city of Tulun based on two change detection methods: Radiometric Rotation Controlled by No-change Axis (*RCNA*) and *Ratioing*, using Sentinel 2 images obtained before the event (19 June 2019) and during the flood peak (29 June 2019). The results obtained by the two methodologies were compared through cross-classification, and a 98% similarity was found in the classification of the areas. The study was validated based on photointerpretation of Google Earth images. The methodology presented proved to be useful for the automatic precession of flooded areas in a straightforward, but rigorous, manner. This allows stakeholders to efficiently manage areas that are buffeted by flooding episodes.

Keywords: urban floods; Radiometric Rotation Controlled by No-change Axis (*RCNA*); *Ratioing*; remote sensing; Tulun

1. Introduction

Global warming has increased the global average temperature, leading to elevated evapotranspiration and humidity, as well as altered rainfall patterns [1]. This warming effect intensifies extreme rainfall events, resulting in more frequent and severe short duration floods in urban areas [2]. Urban microclimates are also being impacted by global warming, with future projections indicating worsening conditions [3].

Rapid urban growth, climate change-induced rainfall variations, heat island effects, and inadequate drainage systems exacerbate the severity of high-intensity rainfall events, causing disruptions in cities and significant socio-economic and environmental impacts [4–6]. Studies suggest that urban flooding will likely worsen due to increasing urbanization, extreme rainfall from climate change, expanding impermeable surfaces, and insufficient city planning [7–9]. Lack of maintenance and upgrades to existing drainage infrastructure further worsen the problem. To mitigate urban flooding, city planners and policymakers should consider implementing sustainable drainage systems (SuDS) and green infrastructure [10]. SuDS mimic natural processes and

improve flood management, while enhancing stormwater quality [11,12]. Green infrastructure provides additional storage capacity for stormwater runoff, enhancing the resilience against urban floods [13]. According to a technical report by TerraTech, an offshoot of the Roscosmos State Corporation for Space Activities, Russia has an area of more than 400,000 km^2 that is susceptible to flooding, including around 700 cities and thousands of villages. Annual flood damage is estimated to exceed EUR 500 million [14]. Tulun, a city developed during the Soviet Union period, experienced a significant population influx, despite being located near the flood-prone Iya River. Climate change has resulted in major flooding, with a return period of approximately 10 years for the Iya River [15]. The last sizeable flood occurred on 29 June 2019, significantly damaging residential areas and infrastructure and leaving thousands homeless [16,17]. Tulun, a city suffering from industrial decline in the post-Soviet period, faces numerous challenges that have contributed to its current state of depression. However, it is crucial to focus on revitalizing cities such as Tulun, with the potential for geographical and economic growth [18]. To achieve this goal, it is essential to map the areas at risk of flooding, identify the flood-prone zones, and monitor the extent of flooding to plan emergency operations and mitigate severe impacts. By so doing, authorities can effectively respond to flood-related crises and implement measures to restore the city's prosperity.

Remote sensing through satellite imagery has proven to be an effective approach for detecting flooded areas, providing critical information to delineate affected zones, evaluate damage, and develop predictive models for vulnerability [19,20]. Several studies have explored flood extent detection, the mapping of inundated areas, and the identification of regions prone to rapid flooding using remote sensing techniques applied to Sentinel imagery. These techniques include non-parametric and supervised learning classification algorithms, unsupervised classification, multi-criteria techniques, and neural networks [21–25]. A review by Shen et al. [26] discusses theories and algorithms of flood inundation mapping using synthetic aperture radar (SAR) data. Another study by Anusha et al. [27] discusses thresholding and unsupervised classification for flood detection and flood mapping using multi-temporal synthetic aperture radar and optical data. A study by Tarpanelli et al. [28] evaluating the effectiveness of Sentinel-1 and Sentinel-2 satellites for flood detection assessment in Europe analyzed 10 years of river discharge data over nearly 2000 sites in Europe and extracted flood events exceeding established thresholds as proxies of riverine inundations. Based on the revisit time of the satellite constellations and cloud coverage, the authors derived the percentage of potential inundation events that were observable by Sentinel-1 and Sentinel-2. The results show that, on average, 58% of flood events are potentially observable by Sentinel-1, while only 28% could be observed by Sentinel-2, due to cloud coverage. Qi Zhang et al. [29] proposed an unsupervised approach for automated flooded area mapping using bi-temporal Sentinel-2 multispectral images. The approach involves extracting spatial–spectral features of the images, before and after the flooding, to construct a change magnitude image (CMI), performing uncertainty analysis on the CMI to obtain certain flood pixels and non-flood pixels as reliable classification samples, using a generalized regression neural network (GRNN) as the core classifier to generate an initial flood map, and applying two-stage post-processing to reduce mapping errors and generate a final flood map.

Based on Sentinel-2 imagery, this study aims to map the flooded area during the extreme rainfall event of 29 June 2019 in Tulun using two change detection methods: Radiometric Rotation Controlled by No-change Axis (*RCNA*) and the *Ratioing*. This study identified asymmetries in the flooded area that affected mostly the central, southwestern, and southeastern regions of Tulun City. The *RCNA* method achieved the highest accuracy in classifying flooded and non-flooded areas. Furthermore, it also showed the different illumination conditions of the images in a less sensitive manner. This methodology contributes to helping the stakeholders quickly and accurately identify the boundaries of flooded areas so that future structural interventions can be implemented.

2. Materials and Methods

2.1. Study Area

Tulun is located on the extreme northwestern area of the Irkutsk-Cheremkhovo plain in the oblast of Irkutsk, southeast of Siberia, Russian Federation, and it represents an area of approximately 13,353 hectares. This city is crossed by the Iya river, a tributary of the Oka river, and is susceptible to flooding when extreme precipitation events occur (Figure 1).
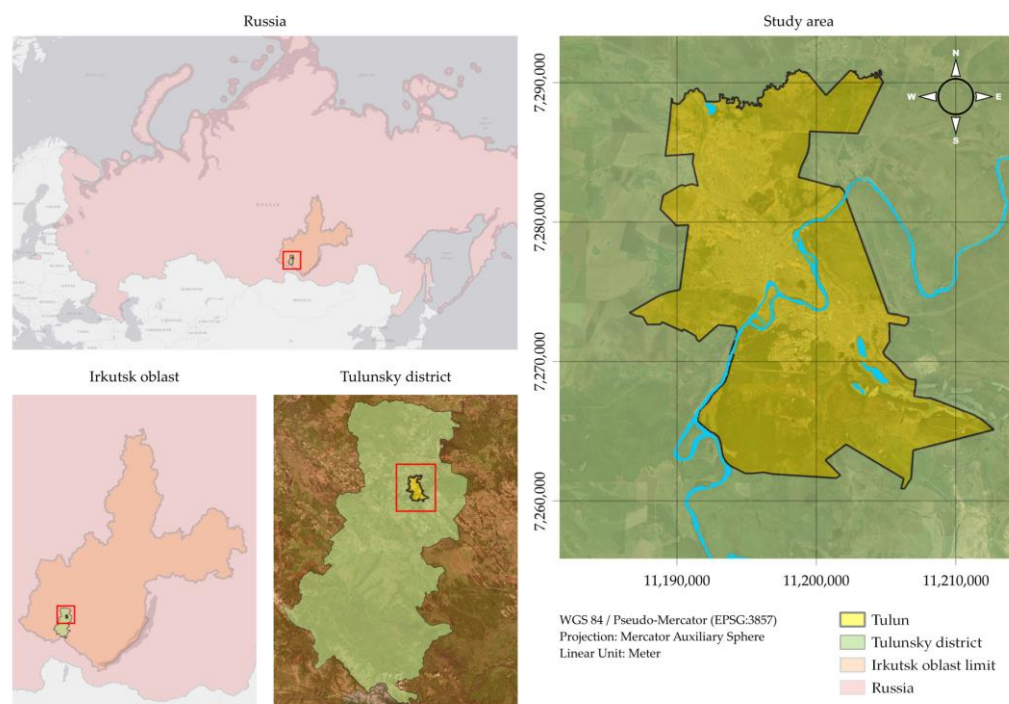
Figure 1. Study area: the Iya River crosses Tulun.

According to the Köppen–Geiger climate classification, the study area is classified by Dfc (subarctic climate), with long, cold (often very cold) winters, and short, warm to cool summers. Tulun's climate is characterized by an average yearly temperature of $-2.2\ ^\circ$C and an annual rainfall average of 438 mm. The heaviest precipitation occurs between May and August. The relief within the city limits is hilly, with absolute elevations ranging from 455 m to 546 m above sea level. Tulun's geologic structure is dominated by sedimentary rocks, which comprise a complex of sediments from the Ordovician, Jurassic, and Quaternary systems. These rocks consist of mudstones, siltstones, limestones, sandstones, quartz schists, and clays. The sedimentary complex is interrupted by eruptive rocks from the Triassic system, including dolerites and dolerite porphyrites. In addition, the Quaternary deposits in Tulun consist of eluvial–diluvial formations in catchments (clays, sandy clays, and occasionally, sands) and alluvial deposits in river valleys (sandy soils) [30].

Tulun, originally a village in the Iya Valley, was founded in the latter half of the 18th century. The city's strategic location along the Trans-Siberian railway and the Vilyuy Federal Highway to Yakutsk enabled it to become a significant trade center, leading to its elevation to city status in 1927. Tulun experienced a boost in its economy with the establishment of several industries, including wood, glass, coal, and a large hydrolysis factory manufacturing chemical products for forestry and agriculture. In 1990, the population of the town reached its peak. However, after the collapse of the Soviet Union, many of these industries shut down, forcing people to emigrate, leading to a decrease in population [15].

2.2. Methodology

For this study, we used Sentinel 2 satellite imagery captured on 19th June and 29th June 2019. The imagery was sourced from Google Earth Engine, and a filter was incorporated

into the script to download only images with a cloud cover of less than 30%. Specifically, we downloaded the blue (B2), green (B3), red (B4), and near-infrared (B8) bands to create the RGB images (true and false colors).

Flood areas were determined based on two change detection methods, Radiometric Rotation Controlled by No-change Axis (*RCNA*) and the *Ratioing*. Both methods were applied to the near-infrared (B8) band of the Sentinel 2 images before the event (19 June 2019) and during the flood peak (29 June 2019) (Figure 2).

Red: B8
Green: B4
Blue: B3

0   5   10   15   20 km
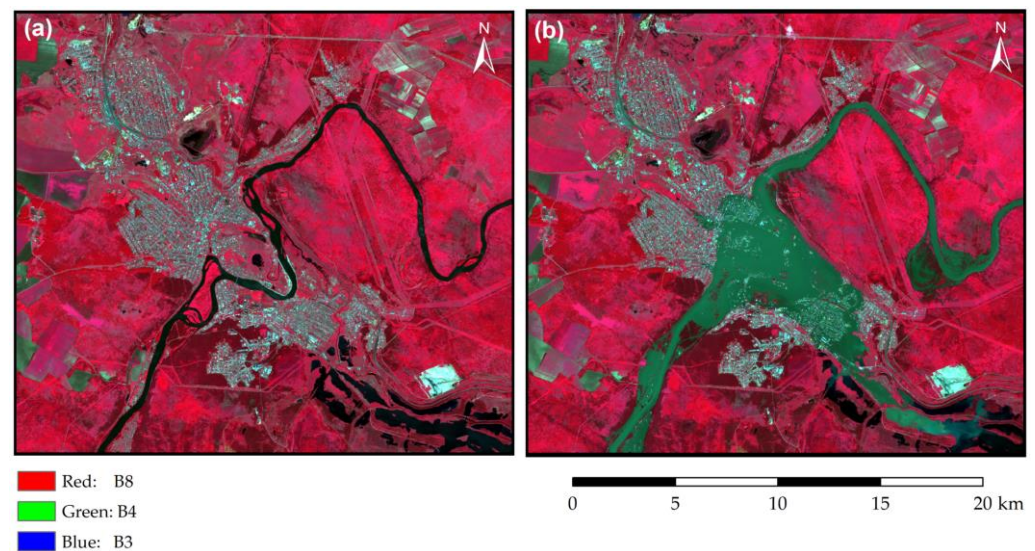
Figure 2. (**a**) Sentinel 2 images before the event (19 June 2019); (**b**) Sentinel 2 images during the flood peak discharge (29 June 2019).

The *RCNA* method, initially proposed by Maldonado et al. [31], is a method for detecting land cover changes based on analyzing radiometric values from two different time periods. It is a flexible method for use with different radiometric conditions caused by, e.g., weather or the effects of seasonal change on solar elevation angle, and it does not require correction for atmospheric effects or sensor differences. Applying a linear regression to areas where no changes have occurred makes it possible to establish a relationship between the radiometric values of the two dates. In this study, the *RCNA* method was applied to water surfaces through a systematic sampling approach. The resulting linear regression, obtained from the points with no change, is defined by Equation (1):

$$im_{date2} = m \, im_{date1} + b \tag{1}$$

where im_{date1} is a radiometric of the no-change pixels obtained before the event, im_{date2} is a radiometric of the no-change pixels for the images obtained after the event, $m = \tan\theta$ is a slope of the no-change axis, θ is angle of the slope, and b is the origin intercept.

The angular parameter (θ) is calculated as the arc tangent of this coefficient. This value represents the angle of the slope of the no-change axis. After calculating the parameter θ and substituting it in Equation (2), the detection images (im_{detec}) and residual images (im_{resid}) are obtained.

$$\begin{bmatrix} im_{resid} \\ im_{detec} \end{bmatrix} = \begin{bmatrix} \cos\theta & \sin\theta \\ -\sin\theta & \cos\theta \end{bmatrix} \times \begin{bmatrix} im_{date1} \\ im_{date2} \end{bmatrix} \tag{2}$$

where im_{detec} is obtained by Equation (3):

$$im_{detec} = \cos\theta \, im_{date2} - \sin\theta \, im_{date1} \tag{3}$$

The im_{detec}, expressed in radiometric levels, shows the changes occurring between the two different times. The lighter tones (high radiometric values) are the pixels that did not exist in im_{date1}, but which appear in im_{date2}, and the darker tones (low radiometric values) are the pixels that disappear between the two different times under analysis.

The *Ratioing* algorithm is a fast method for detecting changes between images at different times by calculating the relationship between the pixels of two images [32]. Still, the success depends on the quality of the atmospheric conditions [33].

Equation (4) expresses the relationship established between the images. The *Ratioing* values will be significantly higher or lower than one, depending on the nature of the changes between the imagery dates. If *Ratioing* values are equal to one, it means that no changes were observed between the two times [34].

$$Rx_{ij}^k = \frac{x_{ij}^k(d2)}{x_{ij}^k(d1)} \tag{4}$$

where $x_{ij}^k(d1)$ is the pixel of row i and column j of band k and time 1, $x_{ij}^k(d2)$ is the pixel of row i and column j of band k and time 2.

Equation (4) requires the application of the arctangent function due to the possibility of encountering a pixel with a value of zero in image $d1$. Without this step, the quotient would be undefined, resulting in incorrect outputs. By utilizing the arctangent function, the resulting values are restricted to angles in radians ranging from 0 to $\pi/2$, ensuring accurate and meaningful results.

In both change detection methods, a thresholding technique of the histogram of the change image was applied. This approach allowed for the effective segmentation of the areas that had experienced changes due to flooding, providing a clear and accurate indication of the extent of the affected regions The pixel values that were shown on the left side of the histogram, i.e., $[minimum, \bar{x} - \sigma]$, were reclassified as one, representing flooded areas. The remaining values were reclassified as zero, i.e., areas with no change, or which experienced change not due to flooding. A cross-classification table was used to compare the results obtained by the two methods, and a spatial analysis was performed to determine the percentage of similarity and difference between the two methods. Based on the Random Points tool of QGIS (version Firenze 3.28.5.1), a set of 100 samples was selected in the study area, and by photointerpretation of the Sentinel 2 image of 29 June 2019 (after the event), the flooded and non-flooded areas were identified. To determine the best method, we extracted the values of the classes obtained by the two change detection methods, constructed an error matrix, and performed accuracy assessments, including overall accuracy, user accuracy, producer accuracy, and Cohen's kappa coefficient, as described by Walz et al. [35].

3. Results and Discussion

The no-changes axes line is defined by an area of 1.5 km^2 located in the southeastern region of the city, as shown in Figure 3.

Equation (5) defines the linear regression shown in Figure 4, where the *X*-axis represents the radiometric values on 19th of June, and the *Y*-axis represents the radiometric values on the 29th of June. The model has an adjustment coefficient of 0.982289, indicating a strong correlation between the two variables.

$$Y = -15.419030 + 0.984043X \tag{5}$$

The results obtained from the *Ratioing* and *RCNA* methods are presented in Figure 5. Grey tones in the figure indicate areas where no changes occurred, black indicates flooded areas, and white represents areas that changed from darker to lighter tones. Figure 5a shows the results obtained through the *Ratioing* method, which reveals changes in the water line and some water bodies. The shift from black to white tones indicates that the method was able to identify the presence of debris (lighter tones) in these areas during

peak flooding, in contrast to the dark color of the water before the flood. Figure 5b presents the results obtained through the *RCNA* method, which classifies the water line and pre-existing water bodies as unchanged (grey tones). However, changes from dark to white tones can be observed in the agricultural area located in the northwest of the city, possibly due to the growth of vegetation (grass) during this period. Both methods were similar in their classification of flooded areas, as indicated by the dark tones. The histogram of the *RCNA* image presents a normal distribution, unlike the slightly positively skewed *Ratioing* histogram. Overall, both methods provide valuable insights into the changes that occurred in the study area, with the *Ratioing* method being more suitable for identifying debris in flooded areas, and the *RCNA* method being more effective in detecting changes in vegetation.

Figure 6 hows the flooded area delineation obtained from the two change detection methods: (a) using the *RCNA* and (b) the *Ratioing* method. The results show similarities between the two methods, as the *Ratioing* methodology only classified a 2% greater area as flooded relative to the results of the *RCNA*.

To compare the results obtained by the two methods, the CROSSTAB tool of TerrSet (version 19.0.6) was used Figure 7. The grey color represents the non-flooded areas classified in both methods (89.5%). The blue color shows the flooded areas classified in both methods (8.6%). Green and red colors relate to the flooded areas classified by only one of the methods, green by *RCNA* (0.6%) and red by *Ratioing* (1.3%).
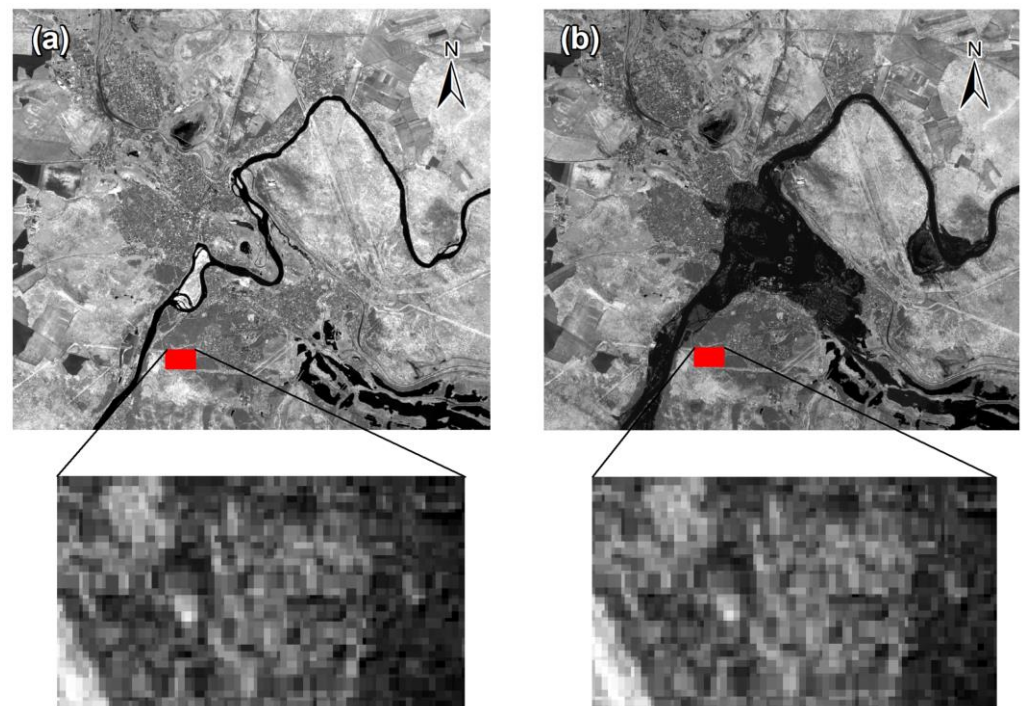

Figure 3. Area selected to set the no-changes axes line: (**a**) before flooding and (**b**) after flooding. The red squares exemplify areas without changes.

Figure 8 displays the random spatial distribution of samples used to validate the results obtained by the two change detection methods. Each sample was associated with a flooded or non-flooded area through photointerpretation. Using the Point Sampling tool of ArcGIS Desktop 10.8 (version 10.8.0.12790), the flooded or non-flooded attribute obtained from each method was also associated with these sampled locations.
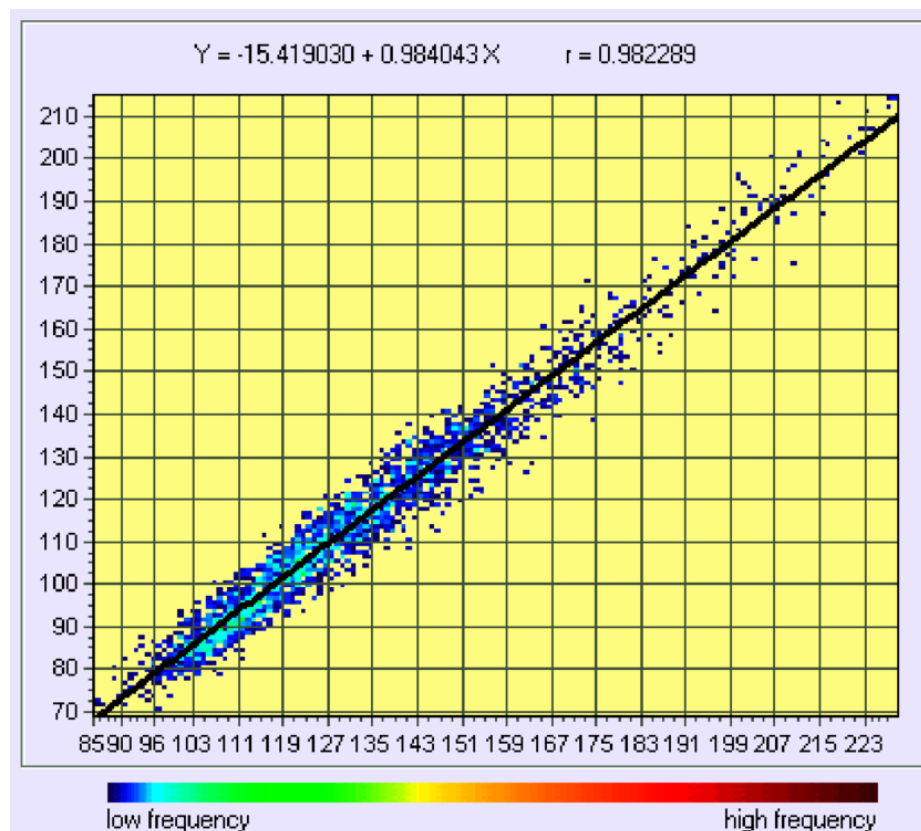
Figure 4. Linear regression, with the *X*-axis representing the radiometric values on the 19th of June, and the *Y*-axis representing the radiometric values on the 29th of June. The line on the plot represents the no-changes axis.
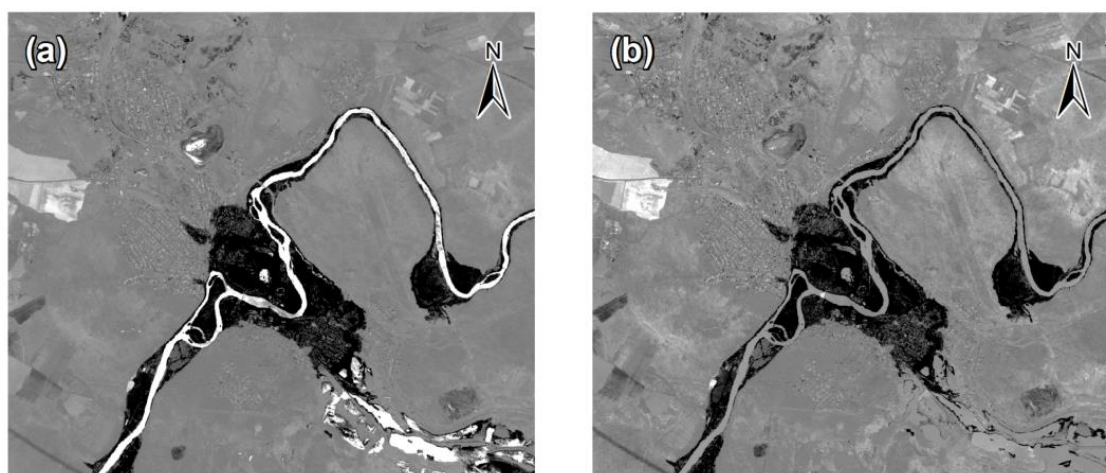

Figure 5. Results of the *Ratioing* and *RCNA* methods: (**a**) change detection image using *Ratioing* method; (**b**) change detection image using *RCNA* method.

For each method, a confusion matrix was constructed to display the classification results. The rows represent the classes that were determined by the methods, while the columns represent the classes that were obtained through photointerpretation. Tables 1 and 2 present the confusion matrices for *Ratioing* and *RCNA*, respectively.
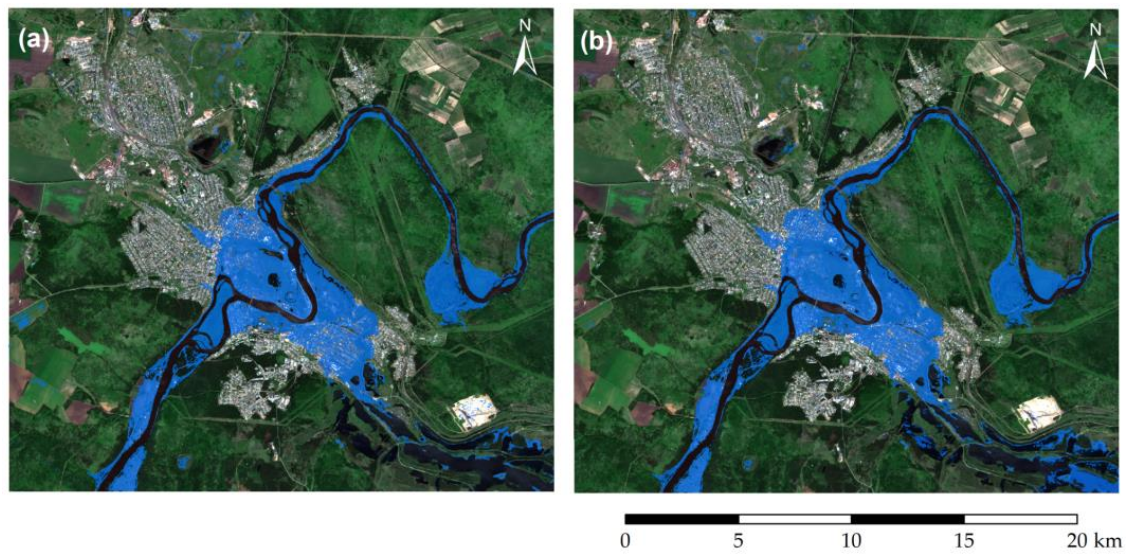
Figure 6. Flooded areas (in blue) for: (**a**) *RCNA* and (**b**) *Ratioing* change detection methods.
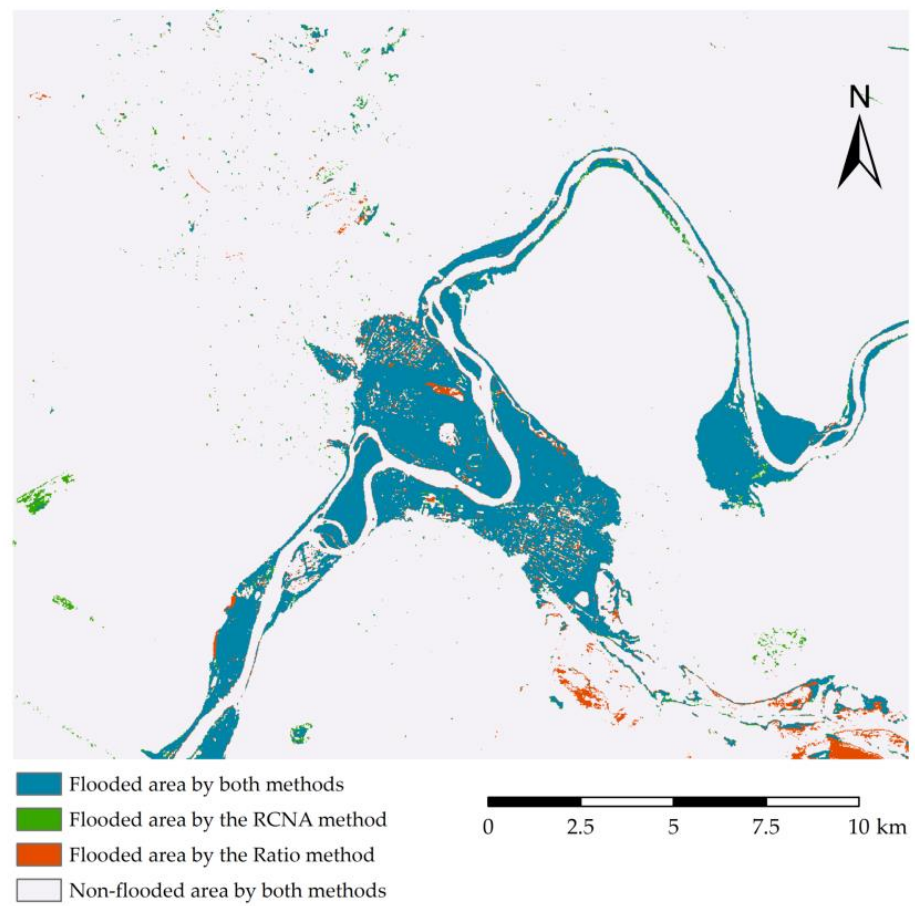
Figure 7. Flooded areas after CROSSTAB operation in TerrSet.
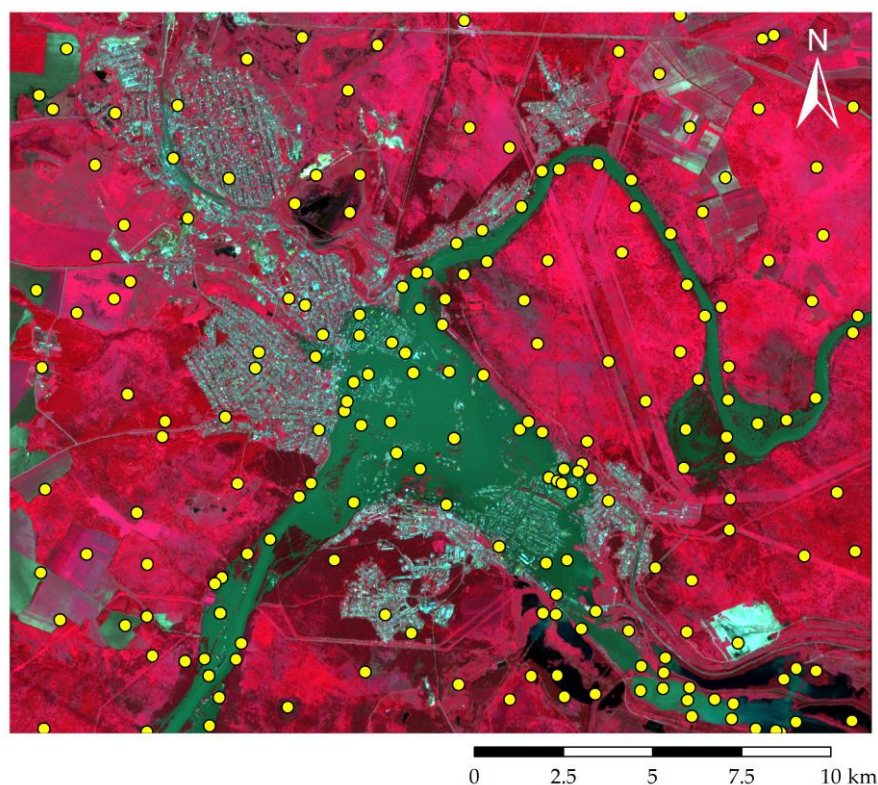
Figure 8. Random validation points for flooded and non-flooded classification.

Table 1. Confusion matrix: *Ratioing* method.

Classes	Flooded Pixels (1)	Non-Flooded Pixels (0)	Total	Errors of Commission	User Accuracy (%)
Flooded (1)	56	27	83	0.33	67.47
Non-flooded (0)	6	111	117	0.05	94.87
Total	62	138	200		
Errors of omission	0.10	0.20			
Producer accuracy (%)	90.32	80.43			

**Table 2.** Confusion matrix: *RCNA* method.

Classes	Flooded Pixels (1)	Non-Flooded Pixels (0)	Total	Errors of Commission	User Accuracy (%)
Flooded (1)	52	15	67	0.22	77.61
Non-flooded (0)	10	123	133	0.08	92.48
Total	62	138	200		
Errors of omission	0.16	0.11			
Producer accuracy (%)	83.87	89.13			

Regarding the accuracy of the classification of the "non-flooded" areas, the methods differ by about 2.4%. However, the *RCNA* method proved to be more reliable in identifying flooded areas, with 77.61% user accuracy, compared to 67.47% using the *Ratioing* method. When it comes to correctly detecting all flooded areas, the *Ratioing* method showed better precision, achieving a 90.32% producer accuracy, while the *RCNA* method achieved 83.87%.

On the other hand, for the non-flooded class, the *RCNA* method outperformed the *Ratioing* method, achieving a higher producer precision score of 89.13% compared to 80.43% obtained by the *Ratioing* method.

Among the methods tested for classifying flooded and non-flooded areas, the *RCNA* demonstrated the highest level of credibility, achieving a Cohen's kappa coefficient of 0.71 and an overall accuracy of 88%. The *Ratioing* method also performed well, with a Cohen's kappa coefficient of 0.65 and an overall accuracy of 84%. Both methods showed a moderate level of agreement in detecting flooded and non-flooded areas, as determined by McHugh's [36] classification, with reliable data comprising between 35% and 63% of the total.

Other studies estimated the flood zone using Modified Normalized Difference Water Index [37] and Modified Shuttle Radar Topography Mission (SRTM) data [38], obtaining results in agreement with ours. The total flood area of Tulun city was estimated to be 12.1 km^2 using the *Ratioing* method, while the *RCNA* method estimated it to be 11.2 km^2. The disparity in the estimated flood area values is attributed to the higher precision of the *RCNA* method in identifying water bodies that existed before the flooding event (see Figure 9).
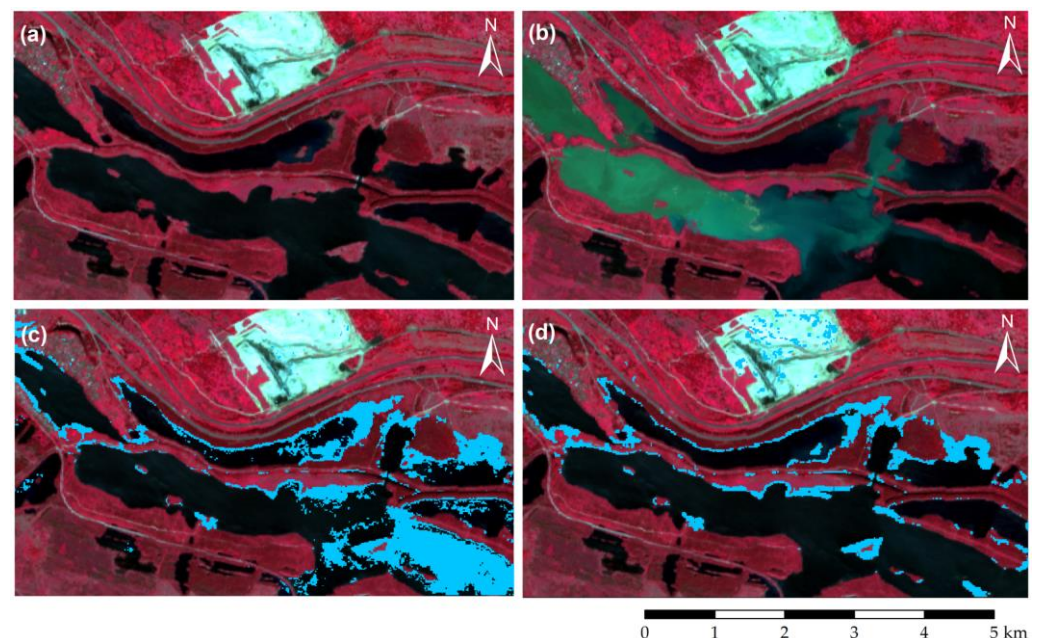

Figure 9. Example of the differences of flooded area detection in southeastern Tulun using the two methods: (**a**) false color image before flooding (19 June 2019); (**b**) false color image after flooding (29 June 2019); (**c**) flooded area detection with *Ratioing*; (**d**) flooded area detection with *RCNA*. In figures (**c**) and (**d**), the flooded areas are highlighted in blue.

This study yielded flooded area values that differ slightly from those published in the technical report by TerraTech. According to their report from 29 June 2019, the inundated area value was 13.1 km^2. However, we have discovered that, unlike in our study, the flood boundary presented in the report contains non-flooded zones within its limits. When accounting for these regions, the *Ratioing* method and the *RCNA* method indicate a total flooded area of approximately 13.6 km^2 and 12.7 km^2, respectively.

An accurate knowledge of the boundaries of flood-prone areas is necessary to develop an urban landscape plan that harmonizes with the natural landscape and incorporates protective engineering structures in order to minimize the flood risk areas in Tulun City. According to Bolshakov [39], the principle of landscape harmony includes urban zoning based on the following considerations: (i) maximum urbanization in flat top areas; (ii) minimal urbanization in floodplains, prioritizing green and leisure spaces; and (iii) moderate

urbanization in slopes, depending on their steepness and the intensity of city development. To replace the constructions located in flood-prone areas, two types of residential areas have been proposed and are currently under construction: (i) family houses in Birch Grove, located on the top of the southern hill on the left bank of the Iya River, between the altitudes of 539 m and 577 m; and (ii) apartments in Coal Miners, located on the right bank between the altitudes of 526 m and 555 m (Figure 10).
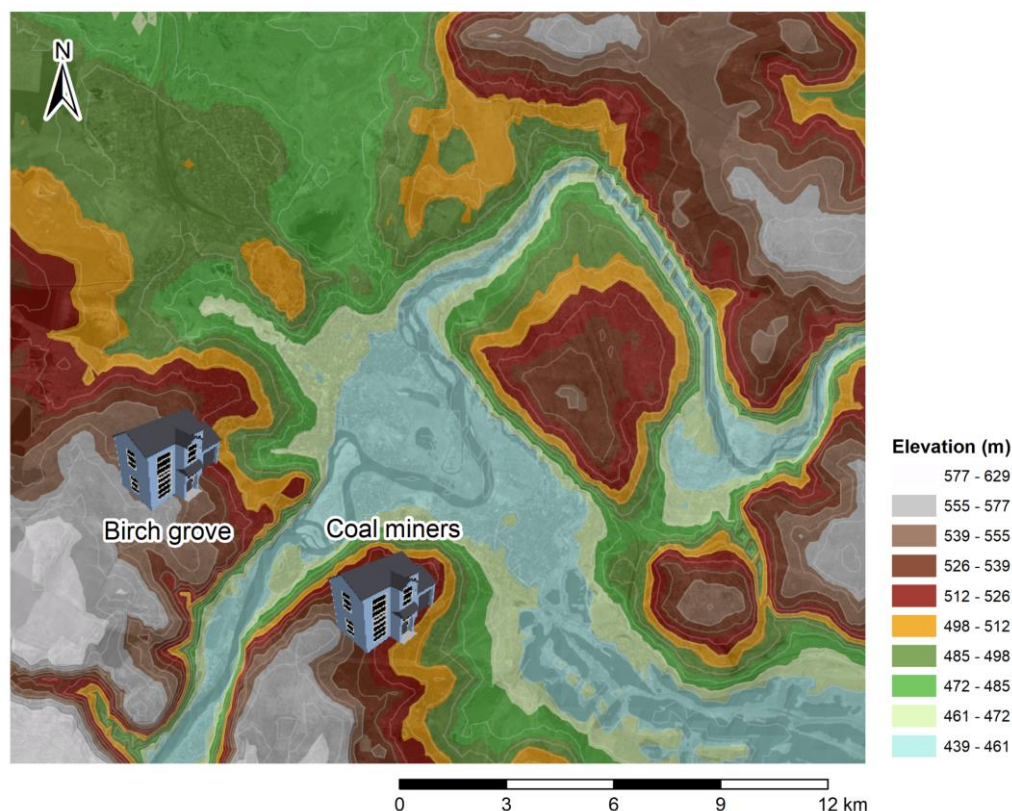

**Figure 10.** Digital Terrain Model and location of new residential areas.

The JSC Hydroproject Institute has designed protection structures to safeguard Tulun City from potential flooding. Two dams, each standing at 15 m high, have been constructed—one located on the north side of the left bank, and the other on the south side of the right bank (see Figure 11). The construction of these dams began in 2020 and is expected to be completed by December 2023, according to the RusHydro group [40].

The R255-Siberia Federal Highway runs through a floodplain area, and the Trans-Siberian Railway follows along the Azey River (Figure 12). According to Kalugin [41] both these infrastructures contribute to an increase in flooding in the urban area and a decrease in the longitudinal slope of the water surface, resulting in a lower streamflow velocity. The road crosses the flooded area and acts as a barrier on the southern zone, while the railway line acts as a barrier on the north, limiting the flooded area from west to east. To address this issue caused by the highway, the JSC Institute of Transportation has proposed a plan for a northern bypass of the city [15]. Although this plan has not yet been implemented, it would be a beneficial sustainability measure, as eliminating this section of the highway could contribute to improved drainage and enhance the landscape conformity.
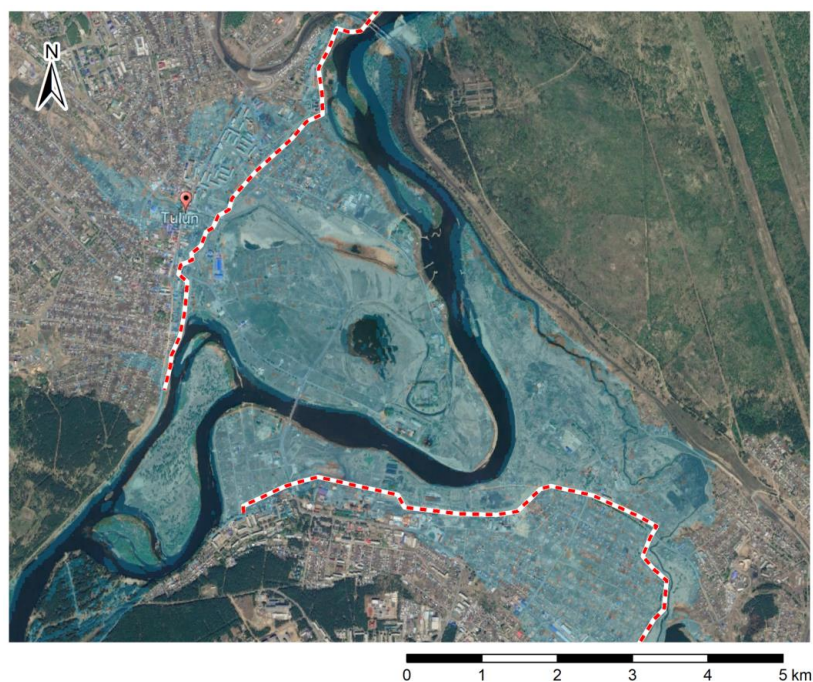
Figure 11. The line on the map indicates the location of dams situated on the left bank, to the north, and the right bank, to the south. Meanwhile, the blue shading represents the flood area estimated using the *RCNA* method.
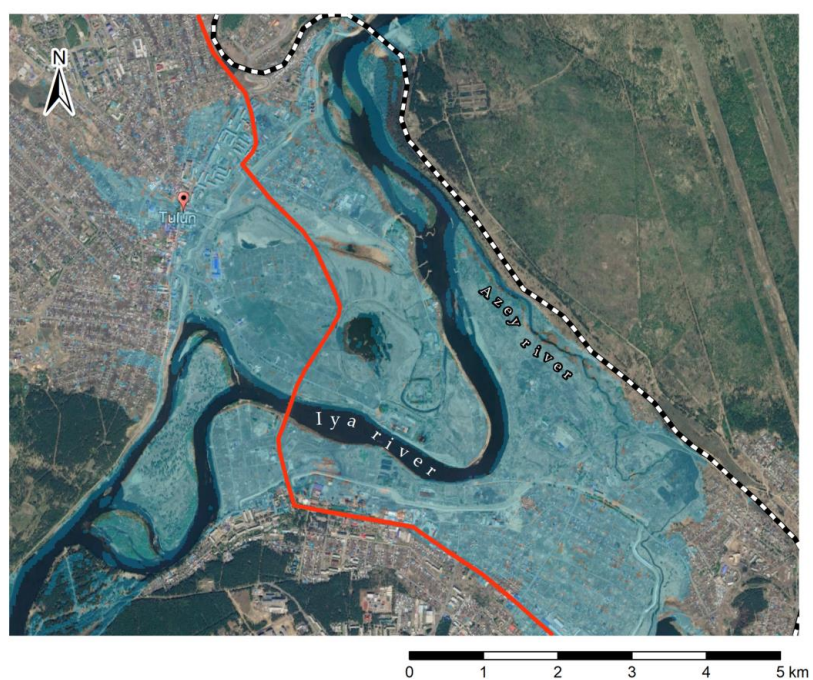
Figure 12. Trans-Siberian Railway (black and white line) and R255-Siberia Federal Highway (red line).

4. Conclusions

In this study, we aimed to determine flood-prone areas following an extreme precipitation event that occurred in Tulun, oblast of Irkutsk, Russian Federation, on 29th June 2019, using the *RCNA* and *Ratioing* classification methods. The total flooded area of the city was estimated to be 12.1 km^2 with the *Ratioing* method and 11.2 km^2 with the *RCNA* method. The delimitation of the flooded area was similar between the two methods, with *Ratioing* classifying a 2% greater area compared to that determined using *RCNA*. We found that

the best method for classifying flooded and non-flooded areas was *RCNA*, with a Cohen's kappa coefficient of 0.71 and an overall accuracy of 88%.

The *Ratioing* method classified some areas as flooded that were actually water bodies (e.g., in the city center) or rivers (e.g., SE zone) before the event. In these areas, there was a slight decrease in near-infrared reflectance at the peak of the flood, which may be explained by differences in illumination and atmospheric conditions during the acquisition of the two images. The positive asymmetry of the histogram of the *Ratioing* image and the adopted thresholding may have contributed to the results. The results obtained using the *RCNA* method showed good accuracy in identifying flood boundaries, which is essential for developing a sustainable urban plan for Tulun City. In the future, we plan to acquire Synthetic-Aperture Radar (SAR) images from Sentinel 1, as they can be obtained under any weather conditions, day or night, and are independent of lighting conditions. Additionally, the reflectance of radar images depend on macroscopic surface characteristics, namely roughness and dielectric properties (related to moisture content). Specifically, to assess the flood depth and the free surface width in rivers and channels, we propose coupling a digital surface model (during the flood, e.g., using Shuttle Radar Topography Mission (SRTM) data) with a DTM (in dry conditions).

Institutional Review Board Statement: Not applicable.

Informed Consent Statement: Not applicable.

Data Availability Statement: Raw data is available upon request.

Conflicts of Interest: The authors declare no conflict of interest.

References

1. Zandalinas, S.I.; Fritschi, F.B.; Mittler, R. Global warming, climate change, and environmental pollution: Recipe for a multifactorial stress combination disaster. *Trends Plant Sci.* **2021**, *26*, 588–599. [CrossRef] [PubMed]
2. Pour, S.H.; Abd Wahab, A.K.; Shahid, S.; Asaduzzaman, M.; Dewan, A. Low impact development techniques to mitigate the impacts of climate-change-induced urban floods: Current trends, issues and challenges. *Sustain. Cities Soc.* **2020**, *62*, 102373. [CrossRef]
3. Halder, B.; Bandyopadhyay, J.; Banik, P. Evaluation of the climate change impact on urban heat island based on land surface temperature and geospatial indicators. *Int. J. Environ. Res.* **2021**, *15*, 819–835. [CrossRef]
4. Zhou, Q.; Leng, G.; Su, J.; Ren, Y. Comparison of urbanization and climate change impacts on urban flood volumes: Importance of urban planning and drainage adaptation. *Sci. Total Environ.* **2019**, *658*, 24–33. [CrossRef] [PubMed]
5. Steensen, B.M.; Marelle, L.; Hodnebrog, Ø.; Myhre, G. Future urban heat island influence on precipitation. *Clim. Dyn.* **2022**, *58*, 3393–3403. [CrossRef]
6. Hassan, B.T.; Yassine, M.; Amin, D. Comparison of urbanization, climate change, and drainage design impacts on urban flashfloods in an arid region: Case study, New Cairo, Egypt. *Water* **2022**, *14*, 2430. [CrossRef]
7. Hammond, M.J.; Chen, A.S.; Djordjević, S.; Butler, D.; Mark, O. Urban flood impact assessment: A state-of-the-art review. *Urban Water J.* **2015**, *12*, 14–29. [CrossRef]
8. Devi, N.N.; Sridharan, B.; Kuiry, S.N. Impact of urban sprawl on future flooding in Chennai city, India. *J. Hydrol.* **2019**, *574*, 486–496. [CrossRef]
9. Chen, K.F.; Leandro, J. A conceptual time-varying flood resilience index for urban areas: Munich city. *Water* **2019**, *11*, 830. [CrossRef]

10. Fletcher, T.D.; Shuster, W.; Hunt, W.F.; Ashley, R.; Butler, D.; Arthur, S.; Trowsdale, S.; Barraud, S.; Semadeni-Davies, A.; Bertrand-Krajewski, J.-L.; et al. SUDS, LID, BMPs, WSUD and more—The evolution and application of terminology surrounding urban drainage. *Urban Water J.* **2015**, *12*, 525–542. [CrossRef]

11. Gimenez-Maranges, M.; Breuste, J.; Hof, A. Sustainable Drainage Systems for transitioning to sustainable urban flood management in the European Union: A review. *J. Clean. Prod.* **2020**, *255*, 120191. [CrossRef]

12. Seyedashraf, O.; Bottacin-Busolin, A.; Harou, J.J. Many-Objective Optimization of Sustainable Drainage Systems in Urban Areas with Different Surface Slopes. *Water Resour. Manag.* **2021**, *35*, 2449–2464. [CrossRef]

13. Green, D.; O'Donnell, E.; Johnson, M.; Slater, L.; Thorne, C.; Zheng, S.; Stirling, R.; Chan, F.K.S.; Li, L.; Boothroyd, R.J. Green infrastructure: The future of urban flood risk management? *Wiley Interdiscip. Rev. Water* **2021**, *8*, e21560. [CrossRef]

14. TerraTech, J.S.C. Space Monitoring of the Flood in Tulun. Status as of July 3. 2019. Available online: https://terratech.ru/news/Tulune.pdf (accessed on 14 February 2023).

15. Bolshakov, A.G. Urban planning analysis of the city of Tulun. *Earth Environ. Sci.* **2021**, *751*, 012041. [CrossRef]

16. Kichigina, N.V. Flood hazard within the basins of the left tributaries of the Angara. *Geogr. Nat. Resour.* **2020**, *41*, 344–353. [CrossRef]

17. Belikov, V.V.; Borisova, N.M.; Glotko, A.V. Numerical Hydrodynamic 2D-Simulation of the Inundation of Tulun Town on the Iya R. during Flood 2019. *Water Resour.* **2021**, *48*, 713–725. [CrossRef]

18. D'yakonov, K.N.; Khoroshev, A.V. Landscape Planning on the Way to Integration in Regional Policy. *Her. Russ. Acad. Sci.* **2022**, *92*, 297–305. [CrossRef]

19. Klemas, V. Remote sensing of floods and flood-prone areas: An overview. *J. Coast. Res.* **2015**, *31*, 1005–1013. [CrossRef]

20. Sadiq, R.; Akhtar, Z.; Imran, M.; Ofli, F. Integrating remote sensing and social sensing for flood mapping. *Remote Sens. Appl. Soc. Environ.* **2022**, *25*, 100697. [CrossRef]

21. Dammalage, T.L.; Jayasinghe, N.T. Land-use change and its impact on urban flooding: A case study on Colombo district flood on May 2016. *Eng. Technol. Appl. Sci. Res.* **2019**, *9*, 3887–3891. [CrossRef]

22. Shahabi, H.; Shirzadi, A.; Ghaderi, K.; Omidvar, E.; Al-Ansari, N.; Clague, J.J.; Geertsema, M.; Khosravi, K.; Amini, A.; Bahrami, S.; et al. Flood detection and susceptibility mapping using sentinel-1 remote sensing data and a machine learning approach: Hybrid intelligence of bagging ensemble based on k-nearest neighbor classifier. *Remote Sens.* **2020**, *12*, 266. [CrossRef]

23. Tanim, A.H.; McRae, C.B.; Tavakol-Davani, H.; Goharian, E. Flood Detection in Urban Areas Using Satellite Imagery and Machine Learning. *Water* **2022**, *14*, 1140. [CrossRef]

24. Farhadi, H.; Esmaeily, A.; Najafzadeh, M. Flood monitoring by integration of Remote Sensing technique and Multi-Criteria Decision Making method. *Comput. Geosci.* **2022**, *160*, 105045. [CrossRef]

25. Hashemi-Beni, L.; Gebrehiwot, A.A. Flood extent mapping: An integrated method using deep learning and region growing using UAV optical data. *IEEE J. Sel. Top. Appl. Earth Obs. Remote Sens.* **2021**, *14*, 2127–2135. [CrossRef]

26. Shen, X.; Wang, D.; Mao, K.; Anagnostou, E.; Hong, Y. Inundation Extent Mapping by Synthetic Aperture Radar: A Review. *Remote Sens.* **2019**, *11*, 879. [CrossRef]

27. Anusha, N.; Bharathi, B. Flood detection and flood mapping using multi-temporal synthetic aperture radar and optical data. *Egypt. J. Remote Sens. Space Sci.* **2020**, *23*, 207–219. [CrossRef]

28. Tarpanelli, A.; Mondini, A.C.; Camici, S. Effectiveness of Sentinel-1 and Sentinel-2 for flood detection assessment in Eu-rope. *Nat. Hazards Earth Syst. Sci.* **2022**, *22*, 2473–2489. [CrossRef]

29. Zhang, Q.; Zhang, P.; Hu, X. Unsupervised GRNN flood mapping approach combined with uncertainty analysis using bi-temporal Sentinel-2 MSI imageries. *Int. J. Digital Earth* **2021**, *14*, 1561–1581. [CrossRef]

30. Akulov, N.I.; Frolov, A.O.; Mashchuk, I.M.; Akulova, V.V. Jurassic deposits of the southern part of the Irkutsk sedimentary basin. *Stratigr. Geol. Correl.* **2015**, *23*, 387–409. [CrossRef]

31. Maldonado, F.D.; Santos, J.R.; Graça, P.M.L. Change detection technique based on the radiometric rotation controlled by no-change axis, applied on a semi-arid landscape. *Int. J. Remote Sens.* **2007**, *28*, 1001–1016. [CrossRef]

32. Minu, S.; Shetty, A. A comparative study of image change detection algorithms in MATLAB. *Aquat. Procedia* **2015**, *4*, 1366–1373. [CrossRef]

33. Hashim, M.; Watson, A.; Thomas, M. An approach for correcting in homogeneous atmospheric effects in remote sensing images. *Int. J. Remote Sens.* **2004**, *25*, 5131–5141. [CrossRef]

34. Lu, D.; Mausel, P.; Batistella, M.; Moran, E. Land-cover binary change detection methods for use in the moist tropical region of the Amazon: A comparative study. *Int. J. Remote Sens.* **2005**, *26*, 101–114. [CrossRef]

35. Yvonne, W.; Maier, S.W.; Dech, S.W.; Conrad, C.; Colditz, R.R. Classification of burn severity using Moderate Resolution Imaging Spectroradiometer (MODIS): A case study in the jarrah-marri forest of southwest Western Australia. *J. Geophys. Res.* **2007**, *112*, G02002. [CrossRef]

36. McHugh, M.L. Interrater reliability: The kappa statistic. *Biochem. Med.* **2012**, *22*, 276–282. [CrossRef]

37. Shalikovsky, A.V.; Lepikhin, A.P.; Tiunov, A.A.; Kurganovich, K.A.; Morozov, M.G. The 2019 Floods in Irkutsk Region. *Водное Хозяйство России Проблемы Технологии Управление* **2019**, *6*, 48–65. [CrossRef]

38. Sutyrina, E.N.; Antonova, T.I. SRTM data application for extrapolation of rating curves (on the example of the Iya river at the Tulun gauge). *Bull. Irkutsk. State Univ. Ser. Earth Sci.* **2022**, *41*, 140–150. [CrossRef]

39. Bolshakov, A.G. Principles of reconstruction of a small depressive city on the example of Tulun. *Earth Environ. Sci.* **2021**, *751*, 012040. [CrossRef]
40. RusHydro Group, JSC Institute Hydroproject. 2019. Available online: http://www.mhp.rushydro.ru/press/publications/113441.html (accessed on 1 April 2023).
41. Kalugin, A. Process-based modeling of the high flow of a semi-mountain river under current and future climatic conditions: A case study of the Iya River (Eastern Siberia). *Water* **2021**, *13*, 1042. [CrossRef]